1-10-2020

# What Can We Learn From X-Ray Fluorescence Core Scanning Data? A Paleomonsoon Case Study

Daniel Gebregiorgis
*Georgia State University*, dgebregiorgis@gsu.edu

Liviu Giosan
*Woods Hole Oceanographic Institution*, lgiosan@whoi.edu

Edmund Hathorne
*GEOMAR Helmholtz Centre for Ocean Research*, ehathorne@geomar.de

Pallavi Anand
*The Open University*, pallavi.anand@open.ac.uk

Katrina Nilsson-Kerr
*The Open University*, katrina.kerr@open.ac.uk

*See next page for additional authors*

## Recommended Citation

## Authors

Daniel Gebregiorgis, Liviu Giosan, Edmund Hathorne, Pallavi Anand, Katrina Nilsson-Kerr, Anna Plaß, Andreas Lückge, Steven Clemens, and Martin Frank

# What Can We Learn From X-Ray Fluorescence Core Scanning Data? A Paleomonsoon Case Study

D. Gebregiorgis[1,2], L. Giosan[3], E. C. Hathorne[2], P. Anand[4], K. Nilsson-Kerr[4], A. Plass[2], A. Lückge[5], S. C. Clemens[6], and M. Frank[2]

[1]Department of Geosciences, Georgia State University, Atlanta, GA, USA, [2]GEOMAR Helmholtz Centre for Ocean Research Kiel, Kiel, Germany, [3]Department of Geology and Geophysics, Woods Hole Oceanographic Institution, Woods Hole, MA, USA, [4]School of Environment, Earth and Ecosystem Sciences, Open University, Milton Keynes, UK, [5]Bundesanstalt für Geowissenschaften und Rohstoffe, Hannover, Germany, [6]Department of Geological Sciences, Brown University, Providence, RI, USA

**Abstract** X-ray fluorescence (XRF) core scanning of marine and lake sediments has been extensively used to study changes in past environmental and climatic processes over a range of timescales. The interpretation of XRF-derived element ratios in paleoclimatic and paleoceanographic studies primarily considers differences in the relative abundances of particular elements. Here we present new XRF core scanning data from two long sediment cores in the Andaman Sea in the northern Indian Ocean and show that sea level related processes influence terrigenous inputs based proxies such as Ti/Ca, Fe/Ca, and elemental concentrations of the transition metals (e.g., Mn). Zr/Rb ratios are mainly a function of changes in median grain size of lithogenic particles and often covary with changes in Ca concentrations that reflect changes in biogenic calcium carbonate production. This suggests that a common process (i.e., sea level) influences both records. The interpretation of lighter element data (e.g., Si and Al) based on low XRF counts is complicated as variations in mean grain size and water content result in systematic artifacts and signal intensities not related to the Al or Si content of the sediments. This highlights the need for calibration of XRF core scanning data based on discrete sample analyses and careful examination of sediment properties such as porosity/water content for reliably disentangling environmental signals from other physical properties. In the case of the Andaman Sea, reliable extraction of a monsoon signal requires accounting for the sea level influence on the XRF data.

**Plain Language Summary** X-ray fluorescence (XRF) core scanning is an important tool of earth scientists to understand the chemical composition of natural archives (e.g., sediment cores) for reconstructing past climate change. The reliability of this tool depends on a detailed understanding of the factors that possibly affect the composition of major and trace elements in sediments and of the translation of the XRF data into elemental concentrations. In paleoceanographic and paleoclimatological studies, ratios of different elements are used to understand climate driven processes such as weathering intensity on land over longer timescale. Some of the widely used ratios of different elements to reconstruct past climate change are, however, influenced by factors that are not directly related to the climate such as amount of rainfall. Here we evaluate these factors by analyzing new data obtained by XRF core scanning of two sediment cores collected from the Andaman Sea, an area dominated by the variability of monsoon rains. We confirm that some of the elemental proxies require careful consideration of sediment properties such as porosity/water content and grain size, and regional changes in sea level, before they can be reliably used to reconstruct past environmental changes.

## 1. Introduction

X-ray fluorescence (XRF) core scanning provides high-resolution nondestructive elemental records allowing investigation of abrupt climate changes otherwise difficult to resolve using time consuming destructive techniques on discrete samples. XRF core scanning generates raw spectroscopic data, which are then converted to element counts and often used as estimates of element concentrations in the sediment. A range of physical factors such as changes in water content, grain size and organic matter impact scanner XRF counts (e.g., Löwemark et al., 2011; Thomson et al., 2006) and elemental ratios are typically employed to overcome

such closed-sum effects (e.g., Weltje & Tjallingii, 2008). However, converting elemental intensities to absolute elemental concentrations is not always straightforward. Previous attempts to calibrate raw XRF core scanner data (expressed as counts per unit time per unit area, or as ratios of counts, count rates, or intensities of elements) to elemental concentration using linear regression models have had variable success (e.g., Tjallingii et al., 2007).

The application of elemental ratios for paleoclimatic and paleoceanographic reconstructions is often based on assumptions of pronounced differences in the mobility of elements during physical erosion and chemical weathering (e.g., Clift et al., 2014). For example, the application of K/Ti and K/Rb as weathering proxies considers the relative proportion of mobile elements such as K against immobile elements such as Ti and Rb (e.g., Clift et al., 2008). Similarly, the application of elemental ratios such as Si/Al (e.g., Meckler et al., 2013), Zr/Rb (e.g., Chen et al., 2006), and Ti/Al (e.g., Tian et al., 2011) invokes the mobility concept to track changes in continental weathering and erosion. The use of elemental ratios such as Ti/Ca and Fe/Ca as terrigenous flux proxies relies on the assumption that the Ti and Fe contents of marine sediments are directly linked to terrigenous (siliciclastic) sediment primarily delivered to the ocean by fluvial and/or eolian transport processes (e.g., Arz et al., 1999; Nace et al., 2014), while Ca intensities reflect changes in the production of calcium carbonate ($CaCO_3$) by marine plankton (e.g., Bahr et al., 2005). XRF-based elemental ratio proxies, such as Ti/Ca, are routinely, therefore, used to reconstruct terrigenous fluxes near continental margins (e.g., Bahr et al., 2008; Kuhnt et al., 2015; Mohtadi et al., 2011). Concentrations of major elements such as Ti and Fe have also been applied on their own to reconstruct changes in continental weathering (e.g., Haug et al., 2001), but dilution processes such as changes in marine biological productivity can affect the interpretation of single element concentrations (e.g., Govin et al., 2012). The Fe content of the sediment could also be impacted by redox processes that lead to migration of iron, with mineral neoformation or expulsion into the water column (e.g., Croudace & Rothwell, 2015). The K content of the sediment has also been applied as a proxy for aridity (Foerster et al., 2012), but the physicochemical processes linking climate with K are just beginning to be fully understood (Foerster et al., 2018). Bahr et al. (2014) used Zr/Al ratios as a proxy for ocean current strength in the Gulf of Cádiz highlighting the potential for transport processes to influence sediment composition. As the technology matures it is necessary to re-evaluate the application of some of the widely used XRF based proxies in paleoclimatology and paleoceanography (Croudace et al., 2019; Chawchai et al., 2016). This is particularly relevant for studies of the past Asian monsoon system, which has been investigated by applying a wide-ranging combination of XRF based proxies over a range of time scales (e.g., Clift et al., 2008; Clift et al., 2014; Prasad et al., 2014; Tian et al., 2011).

Here we provide a detailed evaluation of the climate signals recorded in bulk sediment chemistry using XRF core scanning based on a new centimeter-resolution data set, from two long sediment cores (NGHP17 and U1448) retrieved from the Andaman Sea. A multivariate analysis method, principal component analysis (PCA), is applied to construct proxy composites. We employ coherence and phase analysis with respect to the orbital parameters, eccentricity, obliquity (tilt), and precession (ETP), in order to test whether the proxy composites are driven by known parameters such as sea level or monsoon intensity changes. Proxy composite as well as individual records are directly compared to a recently published South Asian monsoon precipitation record reconstructed independently from sea surface temperature and seawater $\delta^{18}O$ ($\delta^{18}Osw$) records from the same location (Gebregiorgis et al., 2018).

## 2. Andaman Sea Settings and Sediment Source Regions

Intense South Asian monsoon precipitation provides more than $360 \times 10^6$ t of sediments annually to the Andaman Sea from the Indo-Burman Ranges. Most of the sediments from the Indo-Burman-Arakan mountain ranges are supplied to the Andaman Sea through Myanmar's major river systems, mainly those of the Irrawaddy (also known as Ayeyawady or Ayeyarwaddy) and Salween (Awasthi et al., 2014; Figure 1). Rocks in the catchment of the Irrawaddy include Cretaceous to mid-Cenozoic flysch of the western Indo-Burman Ranges, Eocene-Miocene-Quaternary sediments of the Myanmar Central Basin, as well as Late Precambrian, and Cretaceous-Eocene metamorphic, basic, and ultrabasic rocks of the Himalayan mountain ranges in southeastern Tibet (e.g., see Figure 1a in Awasthi et al., 2014). The Salween mainly drains the magmatic rocks of the northern Lhasa block and Precambrian to Tertiary sedimentary and metamorphic rocks of the Shan Plateau and the Sibumashau block. The Irrawaddy built large successive deltas filling in the Central
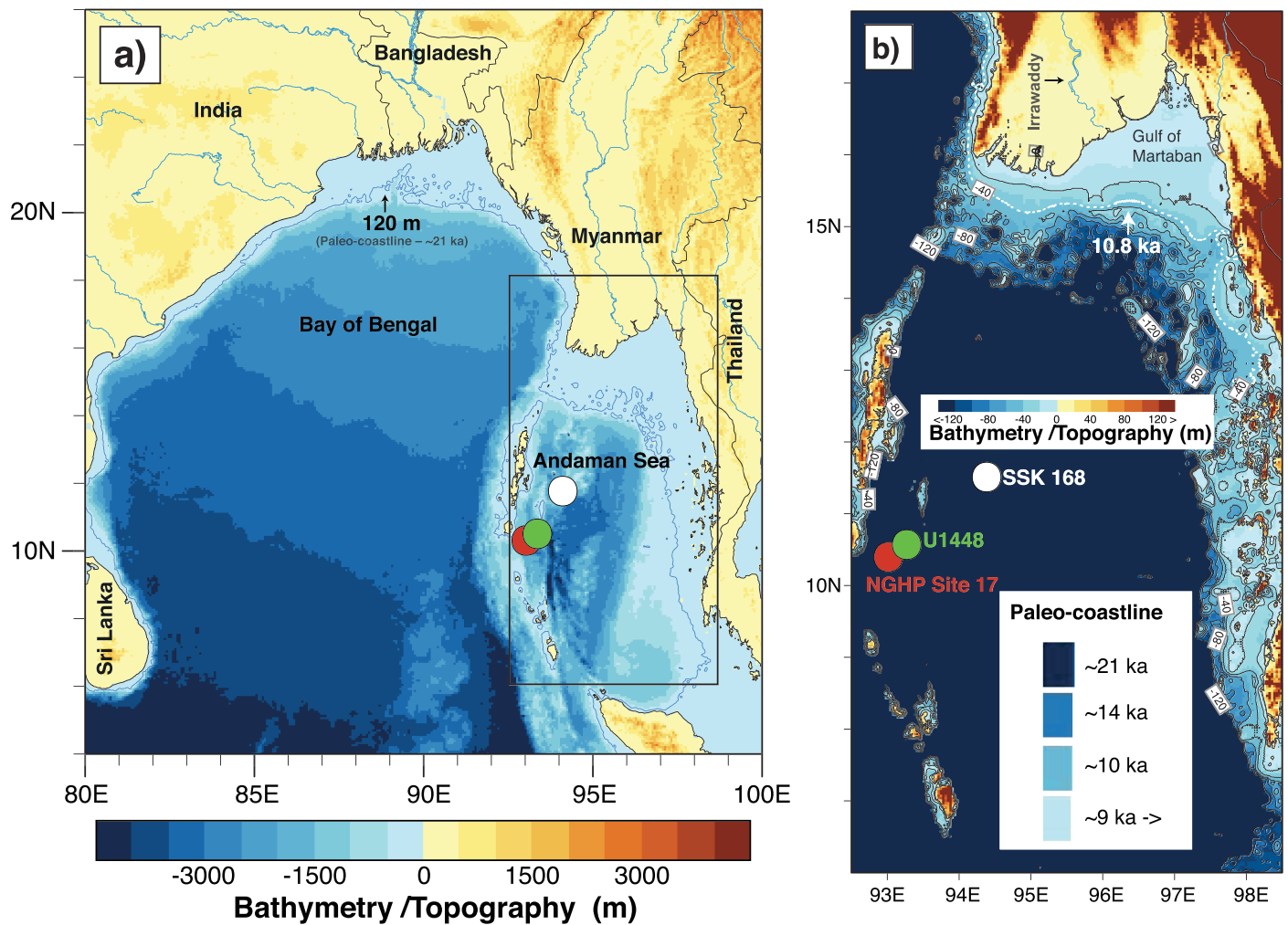
**Figure 1.** Bathymetry and topography map of the (a) Bay of Bengal and (b) Andaman Sea. Blue contour lines mark the 120 m depth interval. Filled circles in (a) and (b) show the locations of the two (NGHP Site 17 and U1448) sediment cores used in the present study and a gravity core (SSK 168) used for comparison. The broken white lines in (a) show the location of the paleo-coast line at 10.8 ka Bathymetry and topography data from NOAA's National Center for Environmental Information (NCEI) (https://www.ngdc.noaa.gov/mgg/global/global.html).

Myanmar basin since Oligocene with the youngest developing since about 9,000 years ago (Giosan et al., 2018), but the comparatively sediment-poor Salween discharges directly into the Gulf of Martaban (e.g., Robinson et al., 2014). Suspended sediment influx from these rivers is transported directly or by resuspension from the continental shelves of Myanmar and Thailand to our core locations mainly via summer monsoon currents (Rao et al., 2005). Roughly 13% of the annual sediment load from the Irrawaddy delta reaches the sea during the northeast winter monsoon (Rodolfo, 1969). Sedimentary rocks of the Indo-Burman-Arakan ranges are composed of easily weatherable material that is delivered to the Andaman Sea during the peak summer monsoon (Damodararao et al., 2016). Thus, the sediments deposited in the Andaman Sea are dominated by influx from the Indo-Burman Ranges and the Central Myanmar basin and are important archives for the investigation of past changes of South Asian monsoon intensity and the resulting weathering inputs (Ali et al., 2015; Colin et al., 1999; Damodararao et al., 2016; Giosan et al., 2018).

## 3. Materials and Methods

### 3.1. Core Descriptions

Sediment core NGHP Site 17 (Latitude 10°45.19′ N; Longitude 93°06.70′E) was retrieved in 2006 in a water depth of 1,356 m in the Andaman Sea using the IODP vessel JOIDES Resolution (Figure 1). The site was cored to over 700 m depth and preserves a late Miocene to recent stratigraphy. Core U1448 (Lat 10°38.03′

N; Long 93°00.00′E) was cored to over 400 mbsf depth and is located 44 km offshore Little Andaman Island (~20 km from NGHP Site 17). The core was retrieved from a water depth of 1,097 m during the IODP Expedition 353 in 2015. Core NGHP Site 17 is dominated by clay-sized (70–100%) and minor amounts of silt-sized (up to 30%) sediments. The biogenic content of the sediments mainly consists of calcareous nanno-fossils and makes up 52% to 97% of the total sediment grains (Collett et al., 2008). Core U1448 has a similar lithology. The upper 180 m of core U1448 is composed of late to early Pleistocene greenish gray clayey nan-nofossil ooze with variable proportions of nannofossils and foraminifers (Clemens et al., 2016).

### 3.2. XRF Core Scanning

XRF scanning was performed using Cox Analytical ITRAX and Avaatech XRF core scanners at WHOI (NGHP Site 17) and the University of Kiel (U1448), respectively. Only sections in the U1448 splice constructed with shipboard color and density scanning data were analyzed with the XRF core scanner. NGHP Site 17 was a single hole so all piston cored sections were scanned. Here we compare the data from the last ~1 Myr for which we have an age model (Gebregiorgis et al., 2018). Details of these methods and analytical capabilities of the ITRAX and Avaatech multifunction core scanners were described by Croudace et al. (2006) and Richter et al. (2006), respectively. Sediment cores (NGHP Site 17 and U1448) were kept in cold storage but allowed to equilibrate with room temperature before measurement. At WHOI, XRF scans were performed using a molybdenum tube set at 60 kV and 30 mA with counting times of 10 s. In Kiel, XRF scans were carried out using a molybdenum tube set at 10 and 30 kV and 25 mA with counting times of 10 to 30 s. These scans pro-vided analyses for 16 elements (K, Ca, Ti, Si, Al, V, Cr, Mn, Fe, Cu, Zn, Br, Rb, Rh, Sr, and Zr). Of these ele-ments, Ca is the most abundant with a mean response rate of ~360,000 counts per second (cps). The response rates of other elements such as K, Ti, Si, and Al range from ~40,000 to ~10,000 cps, in that order, and were well above the nominal sensitivity of the instrument. Sediment cores were measured after careful cleaning and scratching off 1–2 mm of sediment and covering of the core surface with SPEXCerti Ultralene® foil. Except the upper ~1.5 m of the core for Site 17 (measured at a step size of 1 mm), all measurements were performed at a step size of 4 mm (Site 17) and 10 mm (U1448). Raw ITRAX spectroscopic data were processed and con-verted to element counts using the Cox Analytical proprietary software. Raw spectroscopic data for the Avaatech scans were processed and converted to element counts using the Iterative Least square software (WIN AXIL Batch) package. There is strong correspondence between the elemental records from NGHP Site 17 and U1448 (i.e., ITRAX and Avaatech XRF data). Only minor differences are observed in the magni-tude of peaks and signal variability while the pattern of sediment composition is replicated in both cores with minimal chronological errors (see supporting information).

### 3.3. XRF Core Scanning Data Calibration

Raw XRF data were calibrated against quantitative analyses of 80 discrete samples spanning the topmost 15 m of the core on a portable XRF (pXRF) at the Open University, Milton Keynes, UK. For these analyses, ~5 g of material was dried and homogenized to a fine powder and was transferred into vials, sealed tightly with non-PVC Clingfilm and placed over the aperture of the X-ray emitter of a pXRF. Elemental calibration was achieved through analysis of in-house and reference powdered rock standards with known elemental concentrations. A set of internal and reference standards were run after every 10 samples for quality control. The precision was generally better than 5% and 1% for trace and major elements, respectively (Nilsson-Kerr et al., 2019). For a subset of 30 samples, the pXRF data was compared with data obtained using Philips PW 2400 and PW 1480 wavelength dispersive spectrometers measured at the Federal Institute for Geosciences and Natural Resources in Hannover, Germany. The abundances of 42 major and trace elements were quan-titatively determined after fusion of the samples with lithium metaborate at 1200 °C for 20 min (sample/ $LiBO_2 = 1/5$). The quality of the results was controlled by analyses of certified reference materials (CRM) (i.e., BCR, Community Bureau of Reference, Brussels). The precision was generally better than $\pm 0.5$ % for major elements and better than 5 % for trace elements. The WD XRF spectrometer and pXRF calibration data sets are tightly correlated and results are indistinguishable irrespective of the calibration data set (not shown here). Samples from high porosity/water content sections have been excluded for the attempt to calibrate lighter elements (i.e., Si and Al) scanning XRF data. But porosity/water content does not affect relatively hea-vier elements (i.e., Ti, Fe, Ca, and K) and the XRF data for these elements were calibrated against 80 discrete samples including samples from the upper core sections (see supporting information). To convert the raw XRF core scan data (given in cps) to elemental concentrations, a robust regression model from the
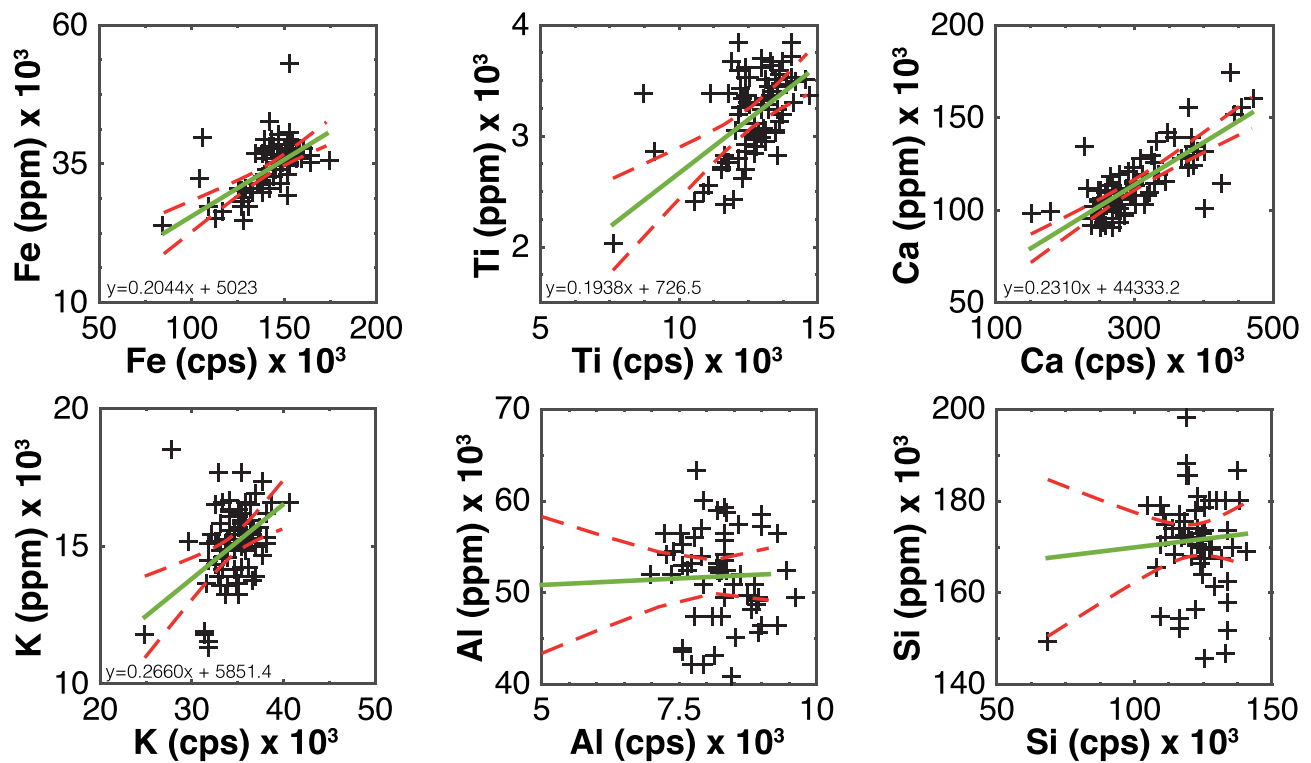
**Figure 2.** Calibration of U1448 XRF elemental concentrations measured by pXRF and applied to XRF core scanning data using a robust regression model. Broken lines (red) represent 95% confidence interval on the fitted values.

Statistics toolbox in MATLAB (R2014b), instead of linear regression models, was applied using the equations shown in Figure 2, based on the pXRF calibration data set (80 samples) (Figure 2). Unlike linear regression models, which provide reliable predictions when the underlying error distribution is Gaussian, robust regression is not overly dependent on this assumption and provides improved results where outliers are common (Rousseeuw & Leroy, 1987). Weltje et al. (2015), however, recommend using multivariate log-ratio calibration equations for calibration purposes, which applies log ratios of element counts and concentrations instead of counts of single elements. We selected the robust regression model in this study as we are particularly interested in patterns of changes in both individual elements and ratios and applying log-ratios of element counts and concentrations did not change the results (see supporting information).

### 3.4. Statistical Analysis

Spectral analyses of the ultra-high-resolution XRF records were performed on an evenly distributed time series using REDFIT (Schulz & Mudelsee, 2002). We used the Arand software package (Howell, 2001) to perform coherence and phase analysis with respect to ETP on the same evenly distributed time series data. Cross-spectral analysis is applied to quantify phase lead and lags and establish causal links between XRF proxy records and potential forcing mechanisms such as sea level and monsoon precipitation. Accordingly, a statistically significant coherence and similar phasing between a proxy time series and either of monsoon precipitation or sea level, for instance, would indicate the presence of a causal relationship between the two records. For example, if a proxy time series leads both monsoon precipitation and sea level by several thousand years over the precession or obliquity band, we can exclude the possibility that proxy record is linearly driven by either of the two. The evolutionary wavelet spectrum is computed using the Matlab codes of Torrence and Compo (Torrence & Compo, 1998) and is available online (paos.colorado.edu/research/wavelets/). The multivariate technique of PCA analysis is used to build composite proxy records via identification of the dominant factors controlling the variability of the proxies. PCA computes new variables, which are linear functions of the original variables known as principal components that can be meaningfully interpreted. PCA was performed on an evenly (linearly interpolated) time axis running from ~0 to 1 Myr in 0.5 kyr intervals. The
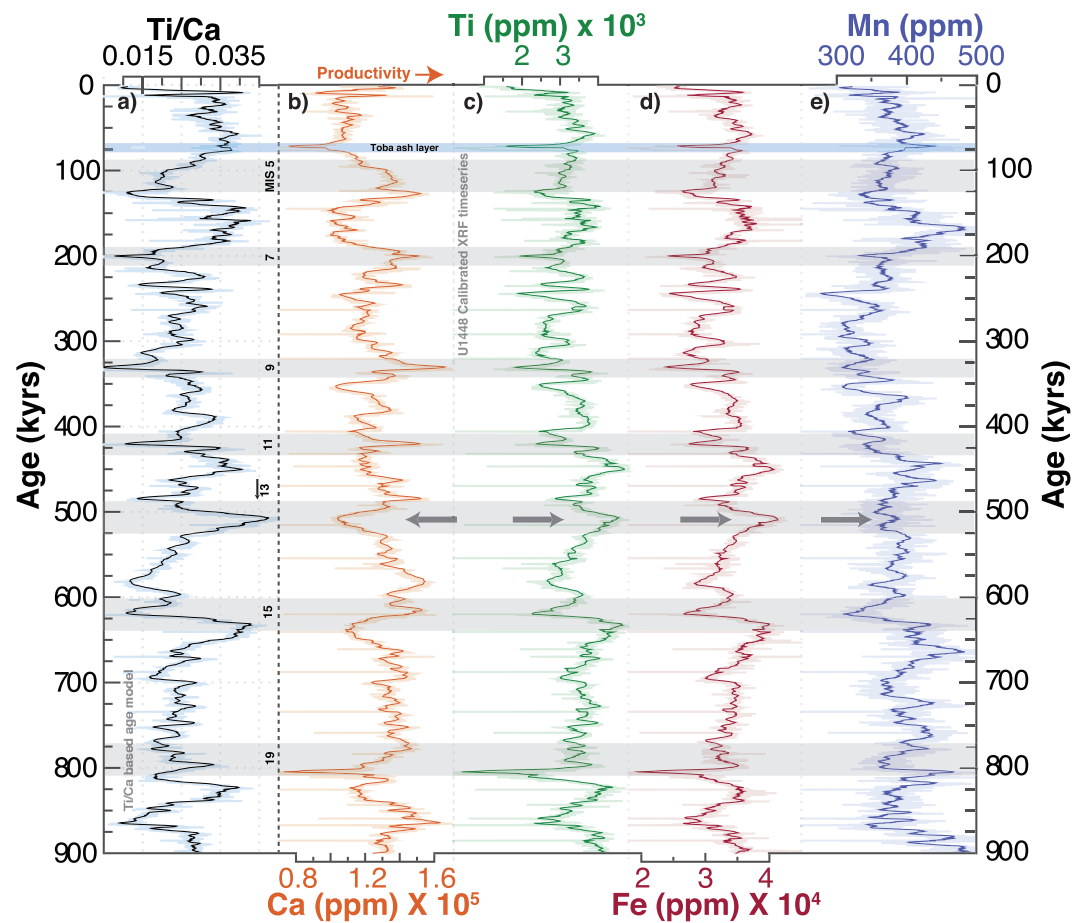
**Figure 3.** U1448 XRF records (a) titanium (Ti)/calcium (Ca) ratios; (b) calcium (Ca) concentration; (c) titanium (Ti) concentration; (d) iron (Fe) concentration; (e) manganese (Mn) concentration. All concentration data are in ppm. Gray bars in (a) show peak interglacial periods identified from the Ti/Ca record. Smoothed lines in all figures are 20-point moving averages.

largest possible variance is extracted in the first principal component while the second principal component explains the maximum part of the remaining variance and so forth. Here PCA operates over the correlation matrix established based on linear relationships between the variables. The purpose of the PCA is to find a set of multivariate constituents dominating the variability in the original data set. PCA analysis is performed using the R package for multivariate analysis (Lê et al., 2008). PCA was carried out using a data set of 18 variables (Ti/Ca, Fe/Ca, Fe/Ti, Mn/Ti, Ti/K, Fe/Mn, Mn/Ca, Mn/K, K/Ca, Fe/Co, Ti (%), Fe (%), Mn (%), K (%), Ca (%) and Si/Al (cps) from U1448, and two additional variables namely Zr/Rb (cps) and K/Rb (cps) from NGHP Site 17).

## 3.5. Grain Size

Following a combination of methods from McCave et al. (1995) and Konert and Vandenberghe (1997), 20 samples from NGHP Site 17 were freeze dried and wet sieved at 63 microns and the fines collected in 10 L plastic bags in large glass jars. After settling for >48 hr the clear water was siphoned off and the fines transferred to 50 mL centrifuge tubes using DI water. Following consolidation by centrifuging at 4,000 rpm for 30 min (2,900 times g with Eppendorf 5810) and siphoning off of excess water, samples were oven dried at 40 °C for 48 hr and then split into two halves. These were dried again in the oven overnight before being weighed and treated with 25 to 30 ml (depending on sample size) of 10% pa $H_2O_2$ solution at room temperature overnight. The samples were then measured for "bulk" composition before being further treated with up to 50 mL 1 M HCl until reaction ceased to remove carbonates and with 20 mL of 0.1 M NaOH to remove opal while agitated in an ultrasonic bath at 60 °C for 1 hr and then left overnight. Before measurement, samples where rinsed
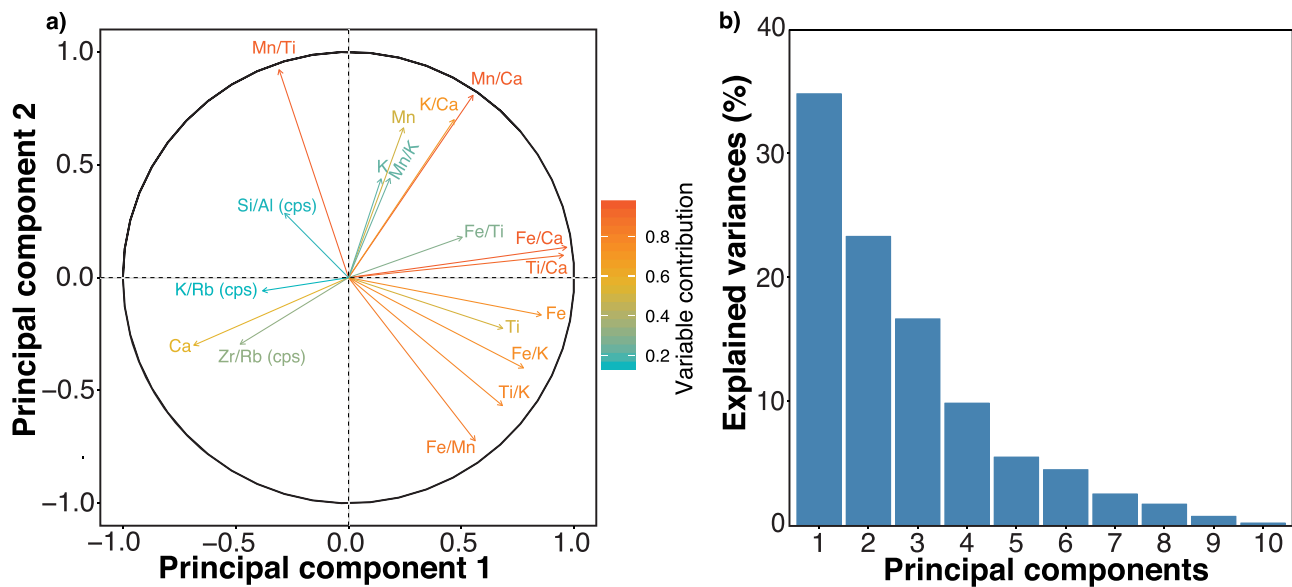
**Figure 4.** Principal component analysis applied to the XRF data matrix. (a) Bi-plot of the first two principal components (PC1 and PC2) explaining 65% of the total variance with input data projections onto the principal components (PCs). (b) Percent variability explained by each principal component. Inputs 1 to 17 represent Ca (%), Fe/Ca (%), Ti/Ca (%), Mn/Ca (%), Co/Ca (%), Fe (%), Mn (%), Ti (%), Co (%), Fe/Mn (%), Fe/Ti (%), Fe/Co (%), Mn/Ti (%), Mn/Co (%), Ti/Co (%), NGHP Site 17 K/Rb (cps), and NGHP Site 17 Zr/Rb (cps).

with DI water and agitated in an ultrasonic bath for >15 min with approx. 25 ml of 0.03 M $Na_6P_6O_{18}$ solution. Immediately before measurement the sample was agitated with a vertex stirrer and the suspension sub sampled with a 1 or 5 ml pipette. Approximately 1 ml of sample suspension was introduced into a FRITSCH laser particle sizer Analysettte-22 NanoTec v2007 to obtain >10% saturation for measurement.

## 4. Results

### 4.1. Quantification of XRF Measurements

The established relationship between raw scanning XRF intensities and the calibration data sets for the robust regression model is shown in Figure 2. The results compare well within ±5 cm sampling offsets and relatively heavier elements such as Ti and Ca particularly align very well (Figure 2). Si and Al show a large discrepancy between conventional XRF core scanning and pXRF analyses (Figure 2), and this is the same for both high and low porosity sections (see supporting information). Linear calibration equations for the same elements except Si and Al are also generally reliable ($r > 0.5$).

The temporal evolution of selected calibrated elemental ratios and concentrations is shown in Figure 3. Maxima and minima of the Ti/Ca, Ca, Ti, and Fe records follow glacial-interglacial cyclicity. Glacial to interglacial cycles are well expressed with a temporal coherence during transitions from glacial to interglacial periods (Figure 3). Distinct peaks in these records mark the onset of major interglacial periods such as Marine Isotope Stage (MIS) 5e and MIS 13. Changes in Mn concentrations, however, are not entirely synchronous with glacial-interglacial cycles (Figure 3). Mn concentration shows the highest values during some glacial stages (e.g., MIS 16, centered at ~670 ka) while the timing of these peaks is not always the same during other glacial stages. For example, the notable peak in Mn concentration centered at ~170 ka lags the beginning of MIS 6 by ~20 kyr (Figure 3).

### 4.2. Composite Proxy Records

PCA analysis identified two distinct principal components, which account for more than 60% of the total variance of the data matrix (Figure 4). The first principal component (PC1) alone represents ~34% of the total variance and is primarily controlled by ratios of Ti/Ca, Fe/Ca, and Ca (%). The second principal component (PC2) accounted for ~24% of the total variance and is mainly controlled by Mn/Ti and Mn/Ca and Mn (%) and Fe/Mn (Figure 4). Lower order PCs are not discussed as each accounted for less than15 % of the total variance within the data set (Figure 4).
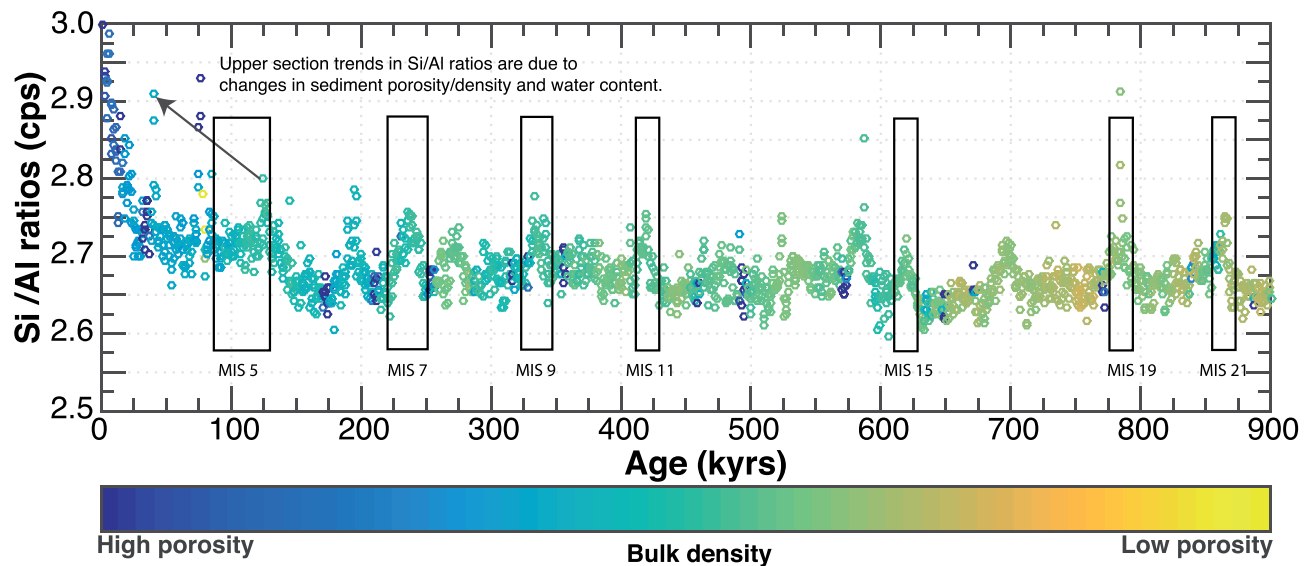
**Figure 5.** Time series of Si/Al ratios with bulk density changes. Dark blue and yellow shading represent low and high sediment porosity, respectively. Note that both time series are on an evenly spaced time axis running from ~0 to 1 Myr in 0.5 kyr intervals.

## 5. Discussion

### 5.1. Factors Influencing Lighter XRF Elements Such as Si and Al

One major advantage of XRF core scanning over destructive elemental composition analysis such as Inductively Coupled Plasma-Mass Spectrometry of discrete samples is that elemental intensities (potentially reflecting changes in concentration) can be measured from the surface of a split sediment core relatively quickly. Previous attempts to calibrating elemental intensities measured by XRF to concentrations applying ordinary least squares linear regression have had varying degrees of success (e.g., Jaccard et al., 2005; Jansen et al., 1998; Tjallingii et al., 2007) and showed lighter elements such as Si and Al are marked by significant differences between wet and dry sample measurements (see Figure 5b in Tjallingii et al., 2007) In all cases, better correlation is achieved with drier samples (Tjallingii et al., 2007). In the present study the calibrations for elements such as Ca, Ti, Mn, Fe, and K are consistent with previous work (e.g., Jaccard et al., 2005; Jansen et al., 1998; Tjallingii et al., 2007). Si and Al data, however, show a large scatter indicating a potential pitfall in the application of Si/Al ratios as proxies (Figure 2).

The use of Si/Al ratios as a weathering proxy is based on the observation that clays are generally enriched in Al and sands are enriched in Si, consistent with the clay to sand ratio of the sediment directly reflecting variations in mineral sorting and physical and chemical weathering processes on land (e.g., Clift et al., 2014; Lupker et al., 2013). Observations show that chemical and physical weathering processes are governed by multiple parameters such as continental precipitation and temperature (e.g., West et al., 2005), which ultimately control the clay to sand ratio of the terrigenous fluxes. Our data show no significant relationship between XRF scans and discrete samples for Si and Al (Figure 2). We conclude that the XRF counts do
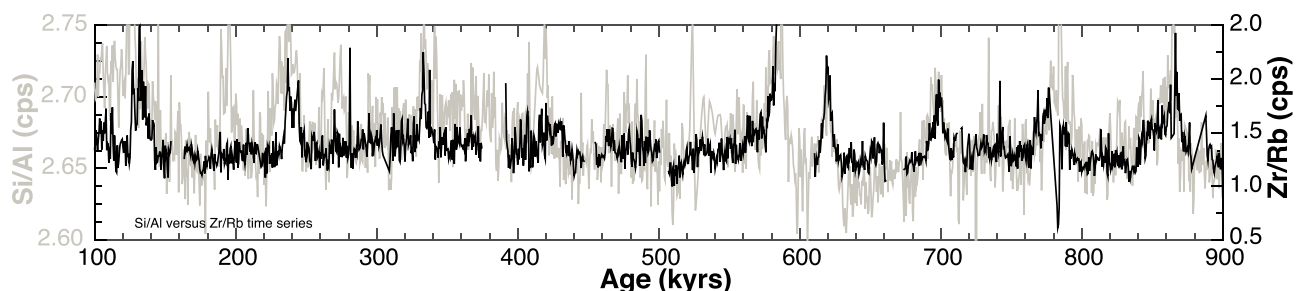


**Figure 6.** Comparison between Si/Al and Zr/Rb ratios from U1448 and NGHP Site 17, respectively.
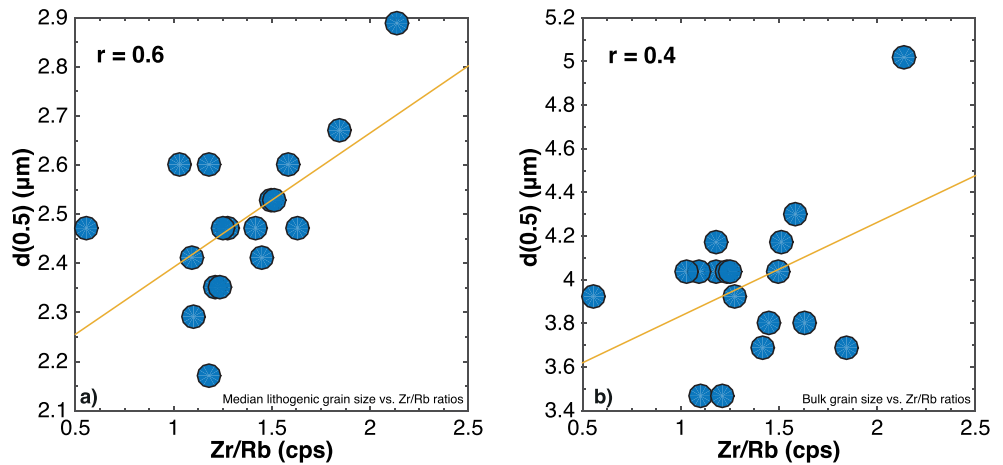
**Figure 7.** Correlation of XRF Zr/Rb with (a) median lithogenic. (b) median bulk (lithogenic plus biogenic) grain size.

not reflect the actual Al or Si content in the sediment but some other factors affect downcore variability of the Si/Al ratio. Low biogenic silica and diatom contents in our sediments (Collett et al., 2008) exclude the possibility that the Si/Al record is significantly controlled by variability in biogenic opal content and fluxes. The organic carbon content of the sediment remained constant at around 1 wt % (Collett et al., 2008) so is unlikely to cause the Si/Al variability. Previous studies reported reduced intensities for lighter elements such as
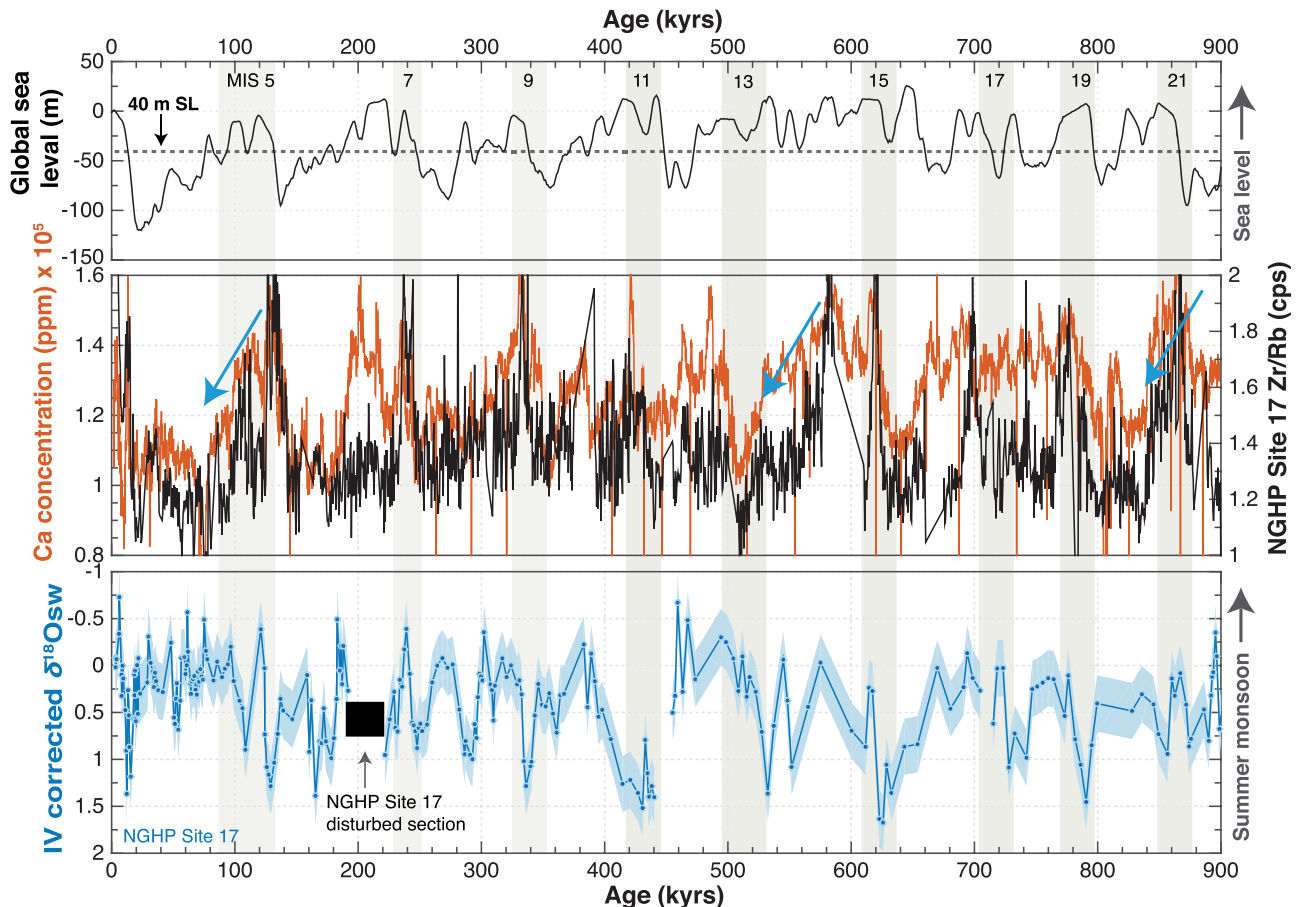


**Figure 8.** Comparison of the global sea level (m) time series (Rohling et al., 2014) with Zr/Rb ratios and Ca concentration changes in the sediment and monsoon precipitation intensity changes inferred from reconstructed $\delta^{18}Osw$ time series over the last ~1 Myr.
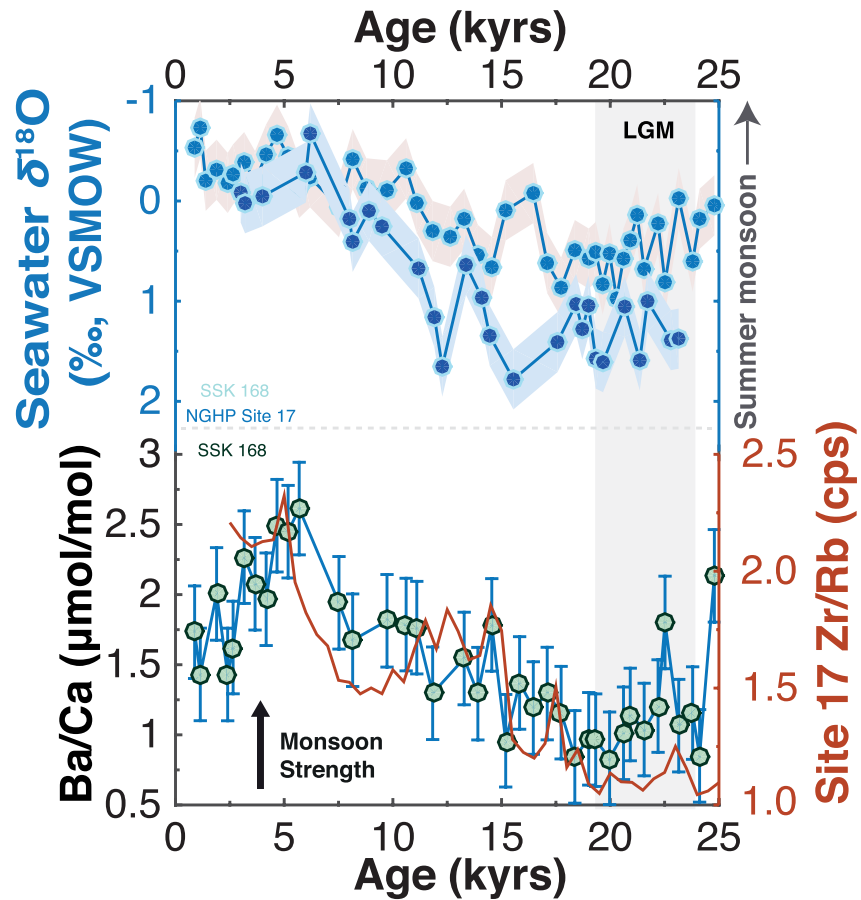
**Figure 9.** Comparison between Zr/Rb ratios (cps) with monsoon precipitation intensity changes inferred from reconstructed $\delta^{18}O_{sw}$ time series from cores SSK 168 (Gebregiorgis et al., 2016) and NGHP Site 17 (Gebregiorgis et al., 2018), and Ba/Ca records from core SSK 168 (Gebregiorgis et al., 2016) in the Andaman Sea over the last ~25 kyr. Envelope in upper figure denotes uncertainty in $\delta^{18}O_{sw}$ reconstructions. Inverted triangles in red and black show radiocarbon dates for core sites NGHP17 and SK168, respectively.

Si and Al when sediments have a high water content while heavier elements are not significantly affected (e.g., Ge et al., 2005; Kido et al., 2006; Tjallingii et al., 2007). A linear relationship between porosity/water content and Si/Al ratios is only observed for the youngest portion of the core back to 60 kyr ($r^2 = 0.5$), but changes in porosity/water content do not control the systematic changes in Si/Al ratios further downcore (Figure 5).

Changes in Si/Al in the older sections of the core largely occur synchronously to those of Zr/Rb (Figure 6) suggesting that common processes may have affected them. Zr and Rb are preferentially enriched in coarser and finer grain size fractions, respectively (e.g., Dypvik & Harris, 2001). To examine if this is the case for our cores, we analyzed grain size spectra for 20 samples from different depth intervals that span the range of the Zr/Rb ratios. Results show that the Zr/Rb ratio is slightly better correlated with changes in median lithogenic grain size than bulk median grain size (i.e., biogenic plus lithogenic) (Figure 7). Note that Si/Al ratios in modern river sediments from the South Asian monsoon region have also shown to be linearly correlated to grain size (e.g., Lupker et al., 2013). In this context the systematic variability in the Si/Al record of the older sections of the core (whether actual or artifact) may reflect in part changes in lithogenic grain size. However, since scanning XRF-estimated Si and Al do not actually correlate to their respective elemental concentrations (Figure 2) the link to lithology remains strenuous. One explanation could be a grain size effect on the measured XRF intensities where changes in the surface roughness of a split core cause systematic errors in the estimated concentrations of light elements (e.g., Baker & Piper, 1976; MacLachlan et al., 2015).
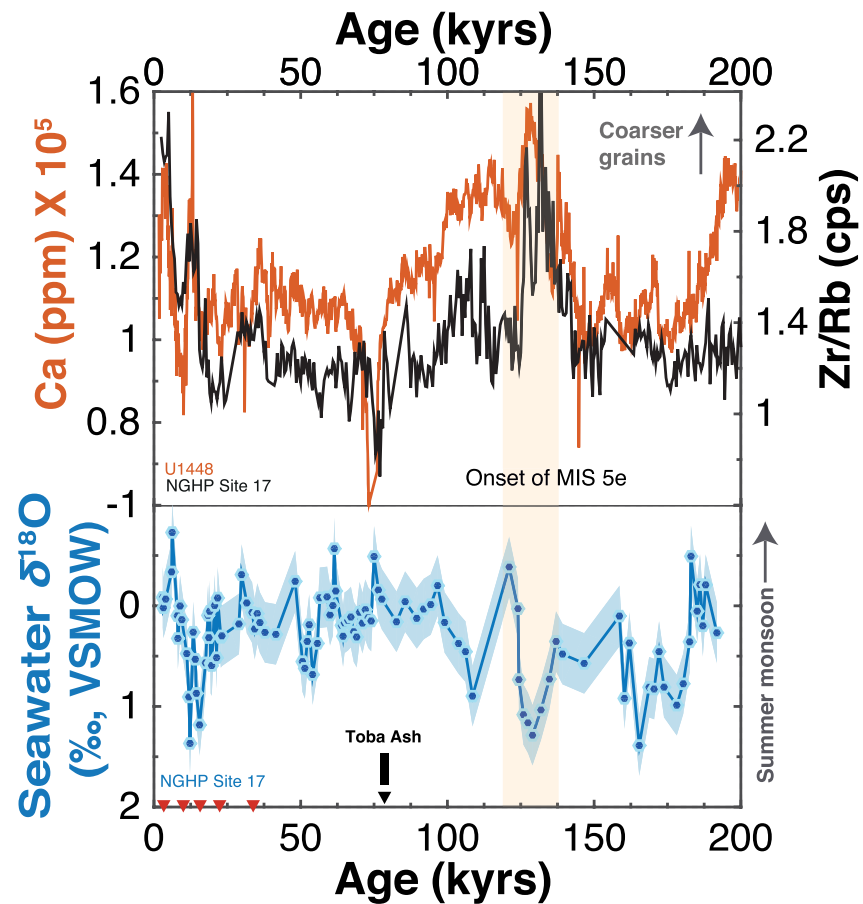
**Figure 10.** Comparison between Zr/Rb ratios and Ca concentration changes in the sediment with monsoon precipitation intensity changes inferred from reconstructed $\delta^{18}O_{sw}$ time series over the last ~200 kyr. Inverted triangles in red show radiocarbon dates for core NGHP Site 17.

## 5.2. Relationships Between Grain Size, Calcium Carbonate, and Monsoon Intensity

The Zr/Rb ratio has previously been applied as a grain size proxy in loess deposits to infer changes in the strength of winds associated with the East Asian winter monsoon (e.g. Chen et al., 2006). On monsoonal continental margin sediments, the Zr/Rb ratio was previously linked to precipitation-driven variations in physical vs. chemical weathering processes on land (Phillips et al., 2014). Comparisons of our Zr/Rb variability records with the monsoon precipitation/runoff record, inferred from ambient seawater $\delta^{18}O_{sw}$ reconstructions based on paired Mg/Ca and $\delta^{18}O$ measurements of planktic foraminifera from the same site, reveals a complex signal (Figure 8). The Zr/Rb record appears to show glacial-interglacial variability, but highs in Zr/Rb ratios do not necessarily coincide with glacial-interglacial cycles and lowest values in Zr/Rb are recorded in some glacial (e.g. MIS 6) and interglacial periods (e.g. MIS 13) (Figure 8). Over the last 25 kyr, however, changes in Zr/Rb ratios are largely synchronous with Ba/Ca and $\delta^{18}O_{sw}$ indicating coupled changes in terrigenous fluxes and runoff from land (Figure 9). However, during the late MIS6, Termination 2 (TII) and at the onset of MIS 5, a marked increase in Zr/Rb ratios coincides with an episode of major monsoon weakening rather than strengthening (Figure 10). One reason for this discrepancy may be the concurrent sea level rise: during the TII transgressive stage both Rb and Zr decrease, with Rb more strongly affected than Zr, reflecting the combined effect of the migration of abundant fine-grained fluvial sources inland and of coarse-grained sediment by waves and tidal currents as the shelf was transgressed (Posamentier et al., 1988; Ramaswamy et al., 2004; Rao et al., 2005). At the scale of our entire record, sea level control may explain high Zr/Rb occurring during all glacial lowstand and transgressive intervals that coincide with periods of decreased monsoon intensity (Figure 8).
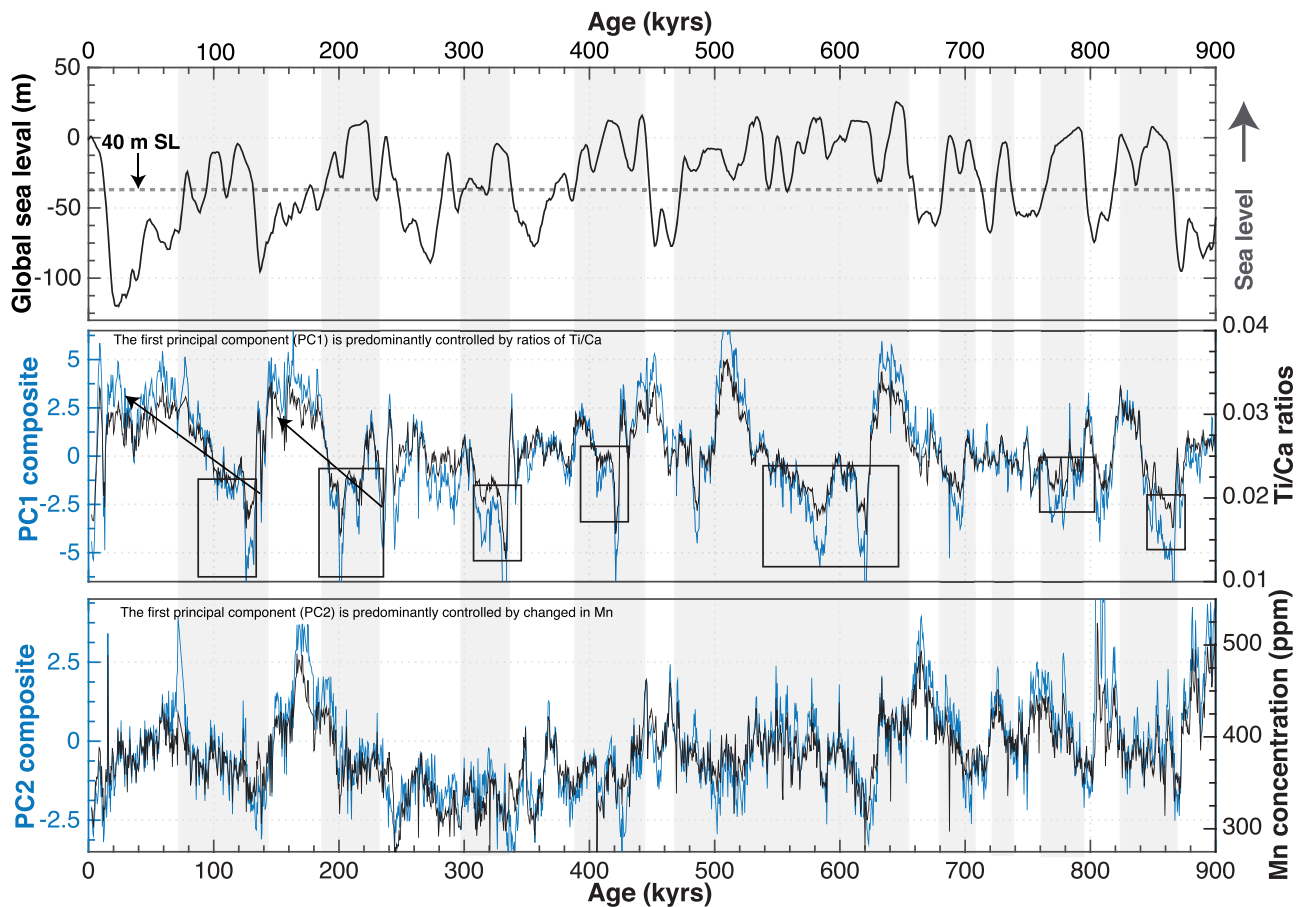
**Figure 11.** Comparison of the global sea level (m) time series (Rohling et al., 2014) with the PC1 and PC2 composite proxy records. Each rectangle shows periods when shelf trapping likely occured at sea level above −40 m.

At most times, changes in Zr/Rb and biogenic calcium carbonate production inferred from changes in Ca concentration are synchronous, with peaks in biogenic production generally matched by increases in Zr/Rb ratios (Figure 8). This suggests that the same processes may have influenced both records (Figure 8). Working in the northwestern Bay of Bengal, offshore the Mahanadi Basin at NGHP Site 19, Phillips et al. (2014) found a strong correlation between Zr/Rb and Ca concentrations. Modern observations show that large summer monsoon-driven freshwater fluxes to the Bay of Bengal lead to a strongly stratified surface layer that curtails vertical mixing thereby inhibiting primary production in the photic zone (e.g. Prasanna Kumar et al., 2002). Looking in more detail at Termination II for example, weak upper ocean stratification triggered by significant weakening of the monsoon (Gebregiorgis et al., 2018) appears to be responsible for the changes in biogenic calcium carbonate production in the Andaman Sea as proposed by Phillips et al. (2014) for the Bay of Bengal (Figure 8). In the NW Bay of Bengal sediments, Zr/Rb correlates with the bulk rather than lithogenic grain size (Phillips et al., 2014). However, the sediments studied by Phillips et al. (2014) had a much lower Ca content than the Andaman Sea cores and in the sediment samples studied here Zr/Rb correlates better with the lithogenic grain size suggesting the Zr/Rb is not directly related to productivity. At NGHP Site 17, the relationship between lithogenic grain size, calcium carbonate production, and monsoon intensity is complex, probably reflecting multiple controls (Figure 8). To attempt to disentangle such complex influences, we employ spectral and PCA analysis to understand how XRF-based proxies relate to known parameters such as sea level or monsoon intensity changes.

### 5.3. Composite Proxy Time Series

XRF-based proxies that may provide estimates of past climate signals over a range of timescales can be directly or indirectly related to the climate system via complex pathways. Our PCA based composite
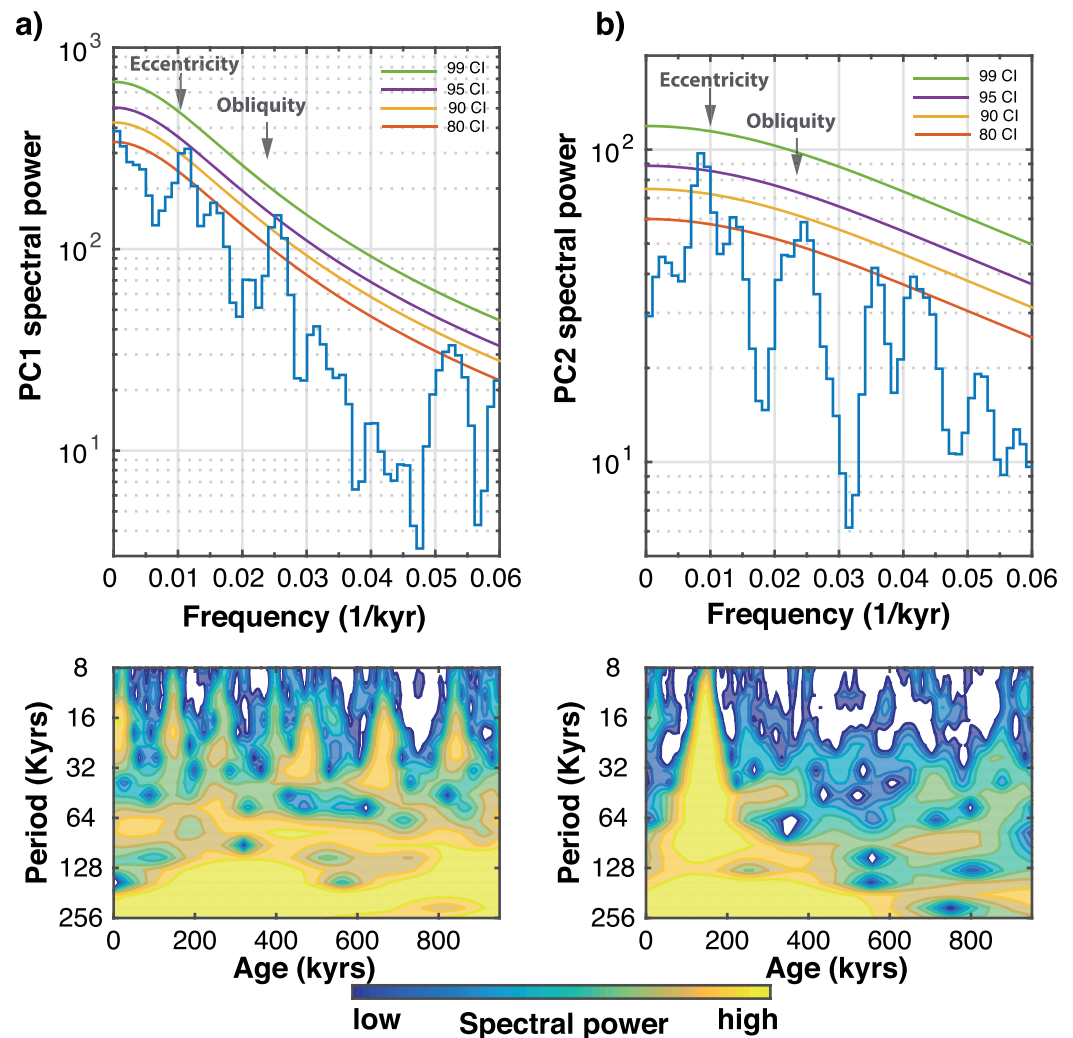
**Figure 12.** a) Redfit spectral analysis of the a) PC1 and b) PC2 time series. Continuous wavelet transform of the PCs are also shown in the same order.

proxy records of XRF based proxies indicate that factors other than the input of terrigenous material, including the dilution of terrigenous elements by calcium carbonate, influence the geochemical composition. Widely used XRF terrigenous proxies such as Ti/Ca and Fe/Ca are predictably susceptible to variations in biological productivity in the Andaman Sea leading to increases in Ca (e.g. Govin et al., 2012), given that there is minimal calcite dissolution at the shallow core depth (e.g. Kolla et al., 1976). The PC1 time series, which represents the variability of Ti/Ca, Fe/Ca and Ca concentration, generally follows glacial-interglacial swings (Figure 11). Spectral analyses of the PC1 composite time series document a dominant periodicity in the ~100 kyr eccentricity band with additional significant contributions of the ~41 kyr obliquity cycle (Figure 12). Continuous wavelet transform of the PC1 time series confirms that strong spectral power is consistently concentrated at frequency bands coinciding with orbital eccentricity (Figure 12). Cross-spectral analysis indicates that none of the records contributing to the PC1 composite are orbitally synchronous with any of the published monsoon intensity records from the Arabian and Andaman seas at the precession band (e.g. Gebregiorgis et al., 2018; Clemens & Prell, 2003, Caley et al., 2011; Figure 13). The PC1 composite, which is strongly influenced by elemental ratios dependent on Ca concentration, appears to be modulated by sea level (Figure 11).
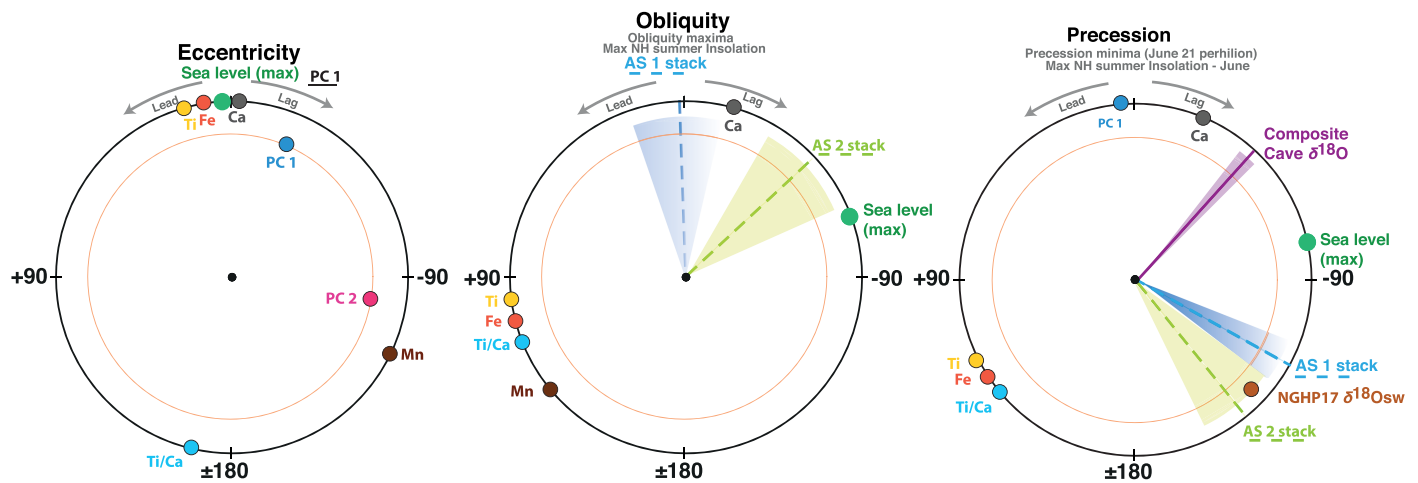
AGU
100
ADVANCING EARTH
AND SPACE SCIENCE

**Geochemistry, Geophysics, Geosystems**

10.1029/2019GC008414

**Figure 13.** Phase wheels summarizing the response of the two PCs and major contributing elements and ratios at the orbital eccentricity (100 kyr), obliquity (41 kyr), and precession (23 kyr). The precession index is defined as $\Delta\varepsilon\sin\omega$ where $\omega$ is the longitude of the perihelion measured from the moving vernal point and $\varepsilon$ is the eccentricity of Earth's orbit around the Sun (Berger & Loutre, 1997; Laskar et al., 1993). Obliquity is the axial tilt of Earth's rotation axis with respect to the orbital plane. In the phase wheel representation the 12 o'clock position is set to precession minima (P min; $\omega = 90°$, 21 June perihelion) and obliquity maxima (O max), respectively. Negative/positive phases are measured in the clockwise/anticlockwise direction and represent phase lags/leads relative to P min or O max. Published records plotted (with shaded phase estimate errors) are the Arabian Sea summer monsoon stacks AS1 (Caley et al., 2011) and AS2 (Clemens & Prell, 2003), the Chinese Sanbao-Hulu cave $\delta^{18}O$ composite (Cheng et al., 2016). Ice volume (IV) corrected $\delta^{18}Osw$ (a measure of surface water salinity) from NGHP Site 17 (Gebregiorgis et al., 2018). The orange circle denotes 80% coherence.

There are two distinct pathways for how sea level would impact the compositions of sediments and thus affect proxies represented by the PC1 composite proxy time series. At lowstands, the extensive continental shelf in front of the Irrawaddy delta becomes exposed, the coastline moves offshore as does the river mouth. Thus the detrital sediment input from rivers will increase at lowstands as the coastline moves seaward, even if the average summer monsoon activity may be significantly weaker (see Figure 1 for the position of paleo-coast over the last 21 kyr). In addition, the "monsoon sediment pump" acts to erode most sediment at times when vegetation is minimal during weak monsoon intervals as long as monsoonal precipitation is still present at the annual time scale (Giosan et al., 2017). Meanwhile during high sea level stands, the previously exposed continental shelf is under water and may inhibit rivers transporting much of their sediment load to offshore basins. For example, increased terrigenous flux inferred from Ti/Ca ratios and the PC1 time series occur both during periods of high (e.g., MIS 13) and low sea levels (e.g., MIS 6) over the last ~1 Myr. From the lead-lag phase change of these records with respect to changes in global ice volume and sea level, we conclude that the monsoon signal in proxy records such as Ti/Ca is overprinted by large changes in sea level modulating monsoon-driven terrigenous flux and calcium biogenic production changes (Figure 10). Despite the fact that the monsoon intensity should strongly influence the nature and timing of sediment delivery to the Andaman Sea (Damodararao et al., 2016), sea level changes appear to largely control the sediment dynamics as predicted (Posamentier et al., 1988).

The PC2 time series accounting for ~24% of the total variance in the data set represents the variability of Mn concentrations and ratios such as Mn/Ti and Mn/Ca. PC2 varies on glacial-interglacial time scales but this is distinctly different from global trends in sea level (Figure 10). Under oxic conditions Mn is delivered to the sediments as Mn (IV) (Mn-oxyhydroxides) (Tribovillard et al., 2006). Under anoxic conditions in sediments and oxygen minimum zones, however, the increased reduction of Mn facilitates the transport of dissolved Mn to oxygenated waters via vertical mixing, where it is reprecipitated and removed from the water via oxidative scavenging. It thus plays a major role in transferring trace metals from the water column to the sediments (Chandana et al., 2017) and the redox-sensitive Mn is indicative of the paleoredox conditions driven by changes in bottom-water oxygen, organic matter fluxes and sedimentation rates. Spectral analyses of the PC2 time series document that the PC2 composite time series is dominated by ~100 kyr eccentricity with strong spectral power consistently concentrated in this frequency band (Figure 11), which is also the case for sea level. Like sea level, the PC2 time series is also coherent at the eccentricity band (Figure 13). The PC2 time series, however, lags maximum eccentricity by ~30 kyr, indicating that the sea level forcing of geochemical

processes is not linear and probably involves thresholds, for example, flooding of the shelf to a sufficient depth where high sedimentation rates could reduce Mn in the sediments.

## 6. Conclusions

Detailed analysis of XRF-based elemental concentration and ratio proxies of two sediment cores from the Andaman Sea highlights some challenges in the application and interpretation of XRF-based elemental time series in paleoclimatology and paleoceanography. The application of noncalibrated data for the lighter elements (such as Si and Al and their ratios) may not be valid given that variations in intensity do not reflect the actual sediment concentrations of these elements. Additionally, the downcore variability of XRF Si/Al is similar to Zr/Rb suggesting that grain size changes influence both parameters. Between the two cores, data replicate very well over the last million years but several of the proxies that are often applied to reflect continental runoff and monsoon intensity changes instead appear to record in part global sea level variability. The application of elemental ratios such as Ti/Ca, Fe/Ca and transition metal concentrations as terrigenous input proxies driven by changes in monsoon strength is complicated given that increasing amounts of terrigenous material are dominantly delivered to the core site during sea level low stands and transgressive stages overprinting the monsoon intensity signal. The present study should motivate further studies seeking corrections for the sea level-related signals in XRF core scanning data to reconstruct paleomonsoon strength, and more generally, paleoclimate.

## References

Ali, S., Hathorne, E. C., Frank, M., Gebregiorgis, D., Stattegger, K., Stumpf, R., et al. (2015). South Asian monsoon history over the past 60 kyr recorded by radiogenic isotopes and clay mineral assemblages in the Andaman Sea. *Geochemistry, Geophysics, Geosystems*, *16*, 505–521. https://doi.org/10.1002/2014GC005586

Arz, H. W., Pätzold, J., & Wefer, G. (1999). Climatic changes during the last deglaciation recorded in sediment cores from the northeastern Brazilian Continental Margin. *Geo-Marine Letters*, *19*(3), 209–218. https://doi.org/10.1007/s003670050111

Awasthi, N., Ray, J. S., Singh, A. K., Band, S. T., & Rai, V. K. (2014). Provenance of the Late Quaternary sediments in the Andaman Sea: Implications for monsoon variability and ocean circulation. *Geochemistry, Geophysics, Geosystems*, *15*, 3890–3906. https://doi.org/10.1002/2014GC005462

Bahr, A., Jiménez-Espejo, F. J., Kolasinac, N., Grunert, P., Hernández-Molina, F. J., Röhl, U., et al. (2014). Deciphering bottom current velocity and paleoclimate signals from contourite deposits in the Gulf of Cádiz during the last 140 kyr: An inorganic geochemical approach. *Geochemistry, Geophysics, Geosystems*, *15*, 3145–3160. https://doi.org/10.1002/2014GC005356

Bahr, A., Lamy, F., Arz, H. W., Kuhlmann, H., & Wefer, G. (2005). Late glacial to Holocene climate and sedimentation history in the NW Black Sea. *Marine Geology*, *214*(4), 309–322. https://doi.org/10.1016/j.margeo.2004.11.013

Bahr, A., Lamy, F., Arz, H. W., Major, C., Kwiecien, O., & Wefer, G. (2008). Abrupt changes of temperature and water chemistry in the late Pleistocene and early Holocene Black Sea. *Geochemistry, Geophysics, Geosystems*, *9*, Q01004. https://doi.org/10.1029/2007GC001683

Baker, E. T., & Piper, D. Z. (1976). Suspended particulate matter: collection by pressure filtration and elemental analysis by thin-film X-ray fluorescence. *Deep Sea Research and Oceanographic Abstracts*, *23*, 181–186.

Berger, A., & Loutre, M. F. (1997). Intertropical latitudes and precessional and half-precessional cycles. *Science*, *278*(5342), 1476–1478. https://doi.org/10.1126/science.278.5342.1476

Caley, T., Malaizé, B., Zaragosi, S., Rossignol, L., Bourget, J., Eynaud, F., et al. (2011). New Arabian Sea records help decipher orbital timing of Indo-Asian monsoon. *Earth and Planetary Science Letters*, *308*(3-4), 433–444. https://doi.org/10.1016/j.epsl.2011.06.019

Chandana, K. R., Bhushan, R., & Jull, A. J. T. (2017). Evidence of poor bottom water ventilation during LGM in the equatorial Indian Ocean. *Frontiers in Earth Science*, *5*, 84. https://doi.org/10.3389/feart.2017.00084

Chawchai, S., Kylander, M. E., Chabangborn, A., Löwemark, L., & Wohlfarth, B. (2016). Testing commonly used X-ray fluorescence core scanning-based proxies for organic-rich lake sediments and peat. *Boreas*, *45*(1), 180–189. https://doi.org/10.1111/bor.12145

Chen, J., Chen, Y., Liu, L., Ji, J., Balsam, W., Sun, Y., & Lu, H. (2006). Zr/Rb ratio in the Chinese loess sequences and its implication for changes in the East Asian winter monsoon strength. *Geochimica et Cosmochimica Acta*, *70*(6), 1471–1482. https://doi.org/10.1016/j.gca.2005.11.029

Cheng, H., Edwards, R. L., Sinha, A., Spötl, C., Yi, L., Chen, S., et al. (2016). The Asian monsoon over the past 640,000 years and ice age terminations. *Nature*, *534*(7609), 640–646. https://doi.org/10.1038/nature18591

Clemens, S. C., Kuhnt, W., LeVay, L. J., Anand, P., Ando, T., Bartol, M., et al. (2016). Expedition 353 summary. *Proceedings of the International Ocean Discovery Program*, *353*, 1–32. https://doi.org/10.14379/iodp.proc.353.101.2016

Clemens, S. C., & Prell, W. L. (2003). A 350,000 year summer-monsoon multi proxy stack from the Owen Ridge, Northern Arabian Sea. *Marine Geology*, *201*(1-3), 35–51. https://doi.org/10.1016/S0025-3227(03)00207-X

Clift, P. D., Hodges, K. V., Heslop, D., Hannigan, R., Van Long, H., & Calves, G. (2008). Correlation of Himalayan exhumation rates and Asian monsoon intensity. *Nature Geoscience*, *1*(12), 875–880. https://doi.org/10.1038/ngeo351

Clift, P. D., Wan, S., & Blusztajn, J. (2014). Reconstructing chemical weathering, physical erosion and monsoon intensity since 25 Ma in the northern South China Sea: A review of competing proxies. *Earth-Science Reviews*, *130*, 86–102. https://doi.org/10.1016/j.earscirev.2014.01.002

Colin, C., Turpin, L., Bertaux, J., Desprairies, A., & Kissel, C. (1999). Erosional history of the Himalayan and Burman ranges during the last two glacial interglacial cycles. *Earth and Planetary Science Letters*, *171*(4), 647–660. https://doi.org/10.1016/S0012-821X(99)00184-3

Collett, T. S., Riedel, M., Cochran, J. R., Boswell, R., Kumar, P., and Sathe, A. V. (2008). Indian continental margin gas hydrate prospects: Results of the Indian National Gas Hydrate Program (NGHP) expedition 01. In *Proceedings of the 6th International conference on Gas Hydrates*. Vancouver, British Columbia, Canada.

Croudace, I. W., Löwemark, L., Tjallingii, R., & Zolitschka, B. (2019). Current perspectives on the capabilities of high resolution XRF core scanners. *Quaternary International*, *514*, 5–15. https://doi.org/10.1016/j.quaint.2019.04.002

Croudace, I. W., Rindby, A., & Rothwell, R. G. (2006). ITRAX: Description and evaluation of a new multi-function X-ray core scanner. *Geological Society, London, Special Publications*, *267*(1), 51–63. https://doi.org/10.1144/GSL.SP.2006.267.01.04

Croudace, I. W., & Rothwell, R. G. (Eds) (2015). *Micro-XRF studies of sediment cores: Applications of a non-destructive tool for the environmental sciences*, (Vol. 17). Dordrecht: Springer.

Damodararao, K., Singh, S. K., Rai, V. K., Ramaswamy, V., & Rao, P. S. (2016). Lithology, monsoon and sea-surface current control on provenance, dispersal and deposition of sediments over the Andaman continental shelf. *Frontiers in Marine Science*, *3*, 118. https://doi.org/10.3389/fmars.2016.00118

Dypvik, H., & Harris, N. B. (2001). Geochemical facies analysis of fine-grained siliciclastics using Th/U, Zr/Rb and (Zr + Rb)/Sr ratios. *Chemical Geology*, *181*(1-4), 131–146. https://doi.org/10.1016/S0009-2541(01)00278-9

Foerster, V., Junginger, A., Langkamp, O., Gebru, T., Asrat, A., Umer, M., et al. (2012). Climatic change recorded in the sediments of the Chew Bahir basin, southern Ethiopia, during the last 45,000 years. *Quaternary International*, *274*, 25–37. https://doi.org/10.1016/j.quaint.2012.06.028

Foerster, V., Deocampo, D. M., Asrat, A., Günter, C., Junginger, A., Krämer, K. H., et al. (2018). Towards an understanding of climate proxy formation in the Chew Bahir basin, southern Ethiopian Rift. *Palaeogeography, Palaeoclimatology, Palaeoecology*, *501*, 111–123. https://doi.org/10.1016/j.palaeo.2018.04.009

Ge, L., Lai, W., & Lin, Y. (2005). Influence of and correction for moisture in rocks, soils and sediments on in situ XRF analysis. *X-Ray Spectrometry: An International Journal*, *34*(1), 28–34. https://doi.org/10.1002/xrs.782

Gebregiorgis, D., Hathorne, E. C., Giosan, L., Clemens, S., Nürnberg, D., & Frank, M. (2018). Southern Hemisphere forcing of South Asian monsoon precipitation over the past~ 1 million years. *Nature Communications*, *9*, 4702. https://doi.org/10.1038/s41467-018-07076-2

Gebregiorgis, D., Hathorne, E. C., Sijinkumar, A. V., Nath, B. N., Nürnberg, D., & Frank, M. (2016). South Asian summer monsoon variability during the last~ 54 kyrs inferred from surface water salinity and river runoff proxies. *Quaternary Science Reviews*, *138*, 6–15. https://doi.org/10.1016/j.quascirev.2016.02.012

Giosan, L., Naing, T., Tun, M. M., Clift, P. D., Filip, F., Constantinescu, S., et al. (2018). On the Holocene evolution of the Ayeyawady megadelta. *Earth Surface Dynamics*, *6*(2), 451–466. https://doi.org/10.5194/esurf-6-451-2018

Giosan, L., Ponton, C., Usman, M., Glusztajn, J., Fuller, D. Q., Galy, V., et al. (2017). Massive erosion in monsoonal central India linked to late Holocene land cover degradation. *Earth surface dynamics*, *5*, 781–789. https://dx.doi.org/10.5194/esurf-5-781-2017

Govin, A., Holzwarth, U., Heslop, D., Ford Keeling, L., Zabel, M., Mulitza, S., et al. (2012). Distribution of major elements in Atlantic surface sediments (36 N 49 S): Imprint of terrigenous input and continental weathering. *Geochemistry, Geophysics, Geosystems*, *13*, Q01013. https://doi.org/10.1029/2011GC003785

Haug, G. H., Hughen, K. A., Sigman, D. M., Peterson, L. C., & Röhl, U. (2001). Southward migration of the intertropical convergence zone through the Holocene. *Science*, *293*(5533), 1304–1308. https://doi.org/10.1126/science.1059725

Howell, P. (2001). *ARAND time series and spectral analysis package for the Macintosh, Brown University*, IGBP PAGES/World Data Center for Paleoclimatology Data Contribution Series, (Vol. 44). Boulder CO, USA: NOAA/NGDC Paleoclimatology Program.

Jaccard, S. L., Haug, G. H., Sigman, D. M., Pedersen, T. F., Thierstein, H. R., & Röhl, U. (2005). Glacial/interglacial changes in subarctic North Pacific stratification. *Science*, *308*(5724), 1003–1006. https://doi.org/10.1126/science.1108696

Jansen, J. H. F., Van der Gaast, S. J., Koster, B., & Vaars, A. J. (1998). CORTEX, a shipboard XRF-scanner for element analyses in split sediment cores. *Marine Geology*, *151*(1-4), 143–153. https://doi.org/10.1016/S0025-3227(98)00074-7

Kido, Y., Koshikawa, T., & Tada, R. (2006). Rapid and quantitative major element analysis method for wet fine-grained sediments using an XRF microscanner. *Marine Geology*, *229*(3-4), 209–225. https://doi.org/10.1016/j.margeo.2006.03.002

Kolla, V., Bé, A. W., & Biscaye, P. E. (1976). Calcium carbonate distribution in the surface sediments of the Indian Ocean. *Journal of Geophysical Research*, *81*(15), 2605–2616. https://doi.org/10.1029/JC081i015p02605

Konert, M., & Vandenberghe, J. E. F. (1997). Comparison of laser grain size analysis with pipette and sieve analysis: a solution for the underestimation of the clay fraction. *Sedimentology*, *44*(3), 523–535.

Kuhnt, W., Holbourn, A., Xu, J., Opdyke, B., De Deckker, P., Röhl, U., & Mudelsee, M. (2015). Southern Hemisphere control on Australian monsoon variability during the late deglaciation and Holocene. *Nature Communications*, *6*, 5916. https://doi.org/10.1038/ncomms6916

Laskar, J., Joutel, F., & Boudin, F. (1993). Orbital, precessional, and insolation quantities for the Earth from-20 Myr to+10 Myr. *Astronomy and Astrophysics*, *270*, 522–533.

Lê, S., Josse, J., & Husson, F. (2008). FactoMineR: An R package for multivariate analysis. *Journal of Statistical Software*, *25*(1), 1–18.

Löwemark, L., Chen, H. F., Yang, T. N., Kylander, M., Yu, E. F., Hsu, Y. W., et al. (2011). Normalizing XRF-scanner data: A cautionary note on the interpretation of high-resolution records from organic-rich lakes. *Journal of Asian Earth Sciences*, *40*(6), 1250–1256. https://doi.org/10.1016/j.jseaes.2010.06.002

Lupker, M., France-Lanord, C., Galy, V., Lavé, J., & Kudrass, H. (2013). Increasing chemical weathering in the Himalayan system since the Last Glacial Maximum. *Earth and Planetary Science Letters*, *365*, 243–252. https://doi.org/10.1016/j.epsl.2013.01.038

MacLachlan, S. E., Hunt, J. E., & Croudace, I. W. (2015). An empirical assessment of variable water content and grain-size on X-ray fluorescence core-scanning measurements of deep sea sediments. In I. W. Croudace & R. G. Rothwell (Eds.), *Micro-XRF Studies of Sediment Cores (vol.1*, pp. 173–185). Dordrecht, Netherlands: Springer.

McCave, I. N., Manighetti, B., & Robinson, S. G. (1995). Sortable silt and fine sediment size/composition slicing: parameters for palaeo-current speed and palaeoceanography. *Paleoceanography*, *10*(3), 593-610. https://doi.org/10.1029/94PA03039

Meckler, A. N., Sigman, D. M., Gibson, K. A., François, R., Martínez-García, A., Jaccard, S. L., et al. (2013). Deglacial pulses of deep ocean silicate into the subtropical North Atlantic Ocean. *Nature*, *495*(7442), 495–498. https://doi.org/10.1038/nature12006

Mohtadi, M., Oppo, D. W., Steinke, S., Stuut, J. B. W., De Pol-Holz, R., Hebbeln, D., & Lückge, A. (2011). Glacial to Holocene swings of the Australian Indonesian monsoon. *Nature Geoscience*, *4*(8), 540–544. https://doi.org/10.1038/ngeo1209

Nace, T. E., Baker, P. A., Dwyer, G. S., Silva, C. G., Rigsby, C. A., Burns, S. J., et al. (2014). The role of North Brazil Current transport in the paleoclimate of the Brazilian Nordeste margin and paleoceanography of the western tropical Atlantic during the late Quaternary. *Palaeogeography, Palaeoclimatology, Palaeoecology*, *415*, 3–13. https://doi.org/10.1016/j.palaeo.2014.05.030

Nilsson-Kerr, K., Anand, P., Sexton, P. F., Leng, M. J., Misra, S., Clemens, S. C., & Hammond, S. J. (2019). Role of Asian summer monsoon subsystems in the inter-hemispheric progression of deglaciation. *Nature Geoscience*, *12*(4), 290–295. https://doi.org/10.1038/s41561-019-0319-5

Paillard, D., Labeyrie, L. D., & Yiou, P. (1996). AnalySeries 1.0: A Macintosh software for the analysis of geophysical time-series. *Eos*, *77*(39), 379. https://doi.org/10.1029/96EO00259

Phillips, S. C., Johnson, J. E., Giosan, L., & Rose, K. (2014). Monsoon influenced variation in productivity and lithogenic sediment flux since 110 ka in the offshore Mahanadi Basin, northern Bay of Bengal. *Marine and Petroleum Geology*, *58*, 502–525. https://doi.org/10.1016/j.marpetgeo.2014.05.007

Posamentier, H. W., Jervey, M. T., & Vail, P. R. (1988). Eustatic controls on clastic deposition I—Conceptual framework. In C. K. Wilgus, B. S. Hastings, C. G. St. Kendall, H. W. Posamentier, C. A. Ross & J. C. Van Wagoner, Editors, *Sea level changes—An integrated approach*, *Special Publication* (vol. 42, pp. 110–124). Tulsa, Oklahoma: Society of Economic Paleontologists and Mineral- ogists (SEPM).

Prasad, S., Anoop, A., Riedel, N., Sarkar, S., Menzel, P., Basavaiah, N., et al. (2014). Prolonged monsoon droughts and links to Indo-Pacific warm pool: A Holocene record from Lonar Lake, central India. *Earth and Planetary Science Letters*, *391*, 171–182. https://doi.org/10.1016/j.epsl.2014.01.043

Prasanna Kumar, S., Muraleedharan, P. M., Prasad, T. G., Gauns, M., Ramaiah, N., De Souza, S. N., et al. (2002). Why is the Bay of Bengal less productive during summer monsoon compared to the Arabian Sea? *Geophysical Research Letters*, *29*(24), 88–1. https://doi.org/10.1029/2002GL016013

Ramaswamy, V., Rao, P. S., Rao, K. H., Thwin, S., Rao, N. S., & Raiker, V. (2004). Tidal influence on suspended sediment distribution and dispersal in the northern Andaman Sea and Gulf of Martaban. *Marine Geology*, *208*(1), 33–42. https://doi.org/10.1016/j.margeo.2004.04.019

Rao, P. S., Ramaswamy, V., & Thwin, S. (2005). Sediment texture, distribution and transport on the Ayeyarwady continental shelf, Andaman Sea. *Marine Geology*, *216*(4), 239–247. https://doi.org/10.1016/j.margeo.2005.02.016

Richter, T. O., Van der Gaast, S., Koster, B., Vaars, A., Gieles, R., de Stigter, H. C., et al. (2006). The Avaatech XRF Core Scanner: Technical description and applications to NE Atlantic sediments. *Geological Society, London, Special Publications*, *267*(1), 39–50. https://doi.org/10.1144/GSL.SP.2006.267.01.03

Robinson, R. A., Brezina, C. A., Parrish, R. R., Horstwood, M. S., Oo, N. W., Bird, M. I., et al. (2014). Large rivers and orogens: The evolution of the Yarlung Tsangpo-Irrawaddy system and the eastern Himalayan syntaxis. *Gondwana Research*, *26*(1), 112-121. https://doi.org/10.1016/j.gr.2013.07.002

Rodolfo, K. S. (1969). Sediments of the Andaman basin, northeastern Indian Ocean. *Marine Geology*, *7*(5), 371–402. https://doi.org/10.1016/0025-3227(69)90014-0

Rohling, E. J., Foster, G. L., Grant, K. M., Marino, G., Roberts, A. P., Tamisiea, M. E., & Williams, F. (2014). Sea-level and deep-sea-temperature variability over the past 5.3 million years. *Nature*, *508*(7497), 477. https://doi.org/10.1038/nature13230

Rousseeuw, P. J., & Leroy, A. M. (1987). *Robust regression and outlier detection*, (Vol. 1). New York: Wiley.

Southon, J., Kashgarian, M., Fontugne, M., Metivier, B., & Yim, W. W. (2002). Marine reservoir corrections for the Indian Ocean and Southeast Asia. *Radiocarbon*, *44*(1), 167–180. https://doi.org/10.1017/S0033822200064778

Schulz, M., & Mudelsee, M. (2002). REDFIT: estimating red-noise spectra directly from unevenly spaced paleoclimatic time series. *Computers & Geosciences*, *28*(3), 421–426. https://doi.org/10.1016/S0098-3004(01)00044-9

Thomson, J., Croudace, I. W., & Rothwell, R. G. (2006). A geochemical application of the ITRAX scanner to a sediment core containing eastern Mediterranean Sapropel units. *Geological Society, London, Special Publications*, *267*(1), 65–77. https://doi.org/10.1144/GSL.SP.2006.267.01.05

Tian, J., Xie, X., Ma, W., Jin, H., & Wang, P. (2011). X-ray fluorescence core scanning records of chemical weathering and monsoon evolution over the past 5 Myr in the southern South China Sea. *Paleoceanography and Paleoclimatology*, *26*, PA4204. https://doi.org/10.1029/2010PA002045

Tjallingii, R., Röhl, U., Kölling, M., & Bickert, T. (2007). Influence of the water content on X ray fluorescence core-scanning measurements in soft marine sediments. *Geochemistry, Geophysics, Geosystems*, *8*, Q02004. https://doi.org/10.1029/2006GC001393

Torrence, C., & Compo, G. P. (1998). A practical guide to wavelet analysis. *Bulletin of the American Meteorological Society*, *79*(1), 61–78. https://doi.org/10.1175/1520-0477(1998)079<0061:APGTWA>2.0.CO;2

Tribovillard, N., Algeo, T. J., Lyons, T., & Riboulleau, A. (2006). Trace metals as paleoredox and paleoproductivity proxies: An update. *Chemical Geology*, *232*(1-2), 12–32. https://doi.org/10.1016/j.chemgeo.2006.02.012

Weltje, G. J., Bloemsma, M. R., Tjallingii, R., Heslop, D., Röhl, U., & Croudace, I. W. (2015). Prediction of geochemical composition from XRF core scanner data: A new multivariate approach including automatic selection of calibration samples and quantification of uncertainties. In *Micro-XRF Studies of Sediment Cores*, (pp. 507–534). Dordrecht: Springer.

Weltje, G. J., & Tjallingii, R. (2008). Calibration of XRF core scanners for quantitative geochemical logging of sediment cores: Theory and application. *Earth and Planetary Science Letters*, *274*(3-4), 423–438. https://doi.org/10.1016/j.epsl.2008.07.054

West, A. J., Galy, A., & Bickle, M. (2005). Tectonic and climatic controls on silicate weathering. *Earth and Planetary Science Letters*, *235*(1-2), 211–228. https://doi.org/10.1016/j.epsl.2005.03.020

## References From the Supporting Information

Lisiecki, L. E., & Raymo, M. E. (2005). A Pliocene-Pleistocene stack of 57 globally distributed benthic δ18O records. *Paleoceanography*, *20*, PA1003. https://doi.org/10.1029/2004PA001071

Paillard, D., Labeyrie, L. D., & Yiou, P. (1996). AnalySeries 1.0: A Macintosh softw are for the analysis of geophysical time-series. *Eos*, *77*(39), 379. https://doi.org/10.1029/96EO00259

Southon, J., Kashgarian, M., Fontugne, M., Metivier, B., & Yim, W. W. (2002). Marine reservoir corrections for the Indian Ocean and Southeast Asia. *Radiocarbon*, *44*(1), 167–180. https://doi.org/10.1017/S0033822200064778